

The inversion of data from very large 3-D ERT mobile surveys.

M.H. Loke^{1*}, N. Papadopoulos², P.B. Wilkinson³, D. Oikonomou^{2,4}, K. Simyrdanis² and D. Rucker⁵

¹ Geotomo Software Sdn Bhd, 115 Cangkat Minden Jalan 6, 11700 Gelugor, Penang, Malaysia.

email : drmhloke@yahoo.com

² Laboratory of Geophysical-Remote Sensing & Archaeoenvironment (GeoSat ReSeArch), Institute for Mediterranean Studies, Foundation for Research and Technology Hellas, Nikiforou Foka 130, 74 100 Rethymno, Crete, Greece.

emails : nikos@ims.forth.gr, doikonomou@ims.forth.gr, ksimirda@ims.forth.gr

³ British Geological Survey, Keyworth, Nottingham, NG12 5GG, U.K.

email : pbw@bgs.ac.uk

⁴ Aristotle University of Thessaloniki, Thessaloniki, Greece.

⁵ hydroGEOPHYSICS Inc., 2302 North Forbes Boulevard, Tucson, AZ 85745, U.S.A.

email : druck8240@gmail.com

* Corresponding author

Keywords : Resistivity inversion, 3-D, segmentation

Publication

Loke, M.H., Papadopoulos, N., Wilkinson, P.B., Oikonomou, D., Simyrdanis, K. and Rucker, D.F., 2020. The inversion of data from very large 3-D ERT mobile surveys. *Geophysical Prospecting*, **68**, 2579-2597.

Abstract

New developments in mobile resistivity meter instrumentation have made it possible to survey large areas with dense data coverage. The mobile system usually has a limited number of electrodes attached to a cable that is pulled along behind an operator so that a large area can be covered within a short time. Such surveys can produce 3-D data sets with hundreds of thousands of electrodes positions and data points. Similarly, the inverse model used to interpret the data can have several hundred thousand cells. It is impractical to model such large data sets within a reasonable time on microcomputers used by many small companies employing standard inversion techniques. We describe a model segmentation technique that subdivides the finite-element mesh used to calculate the apparent resistivity and Jacobian matrix values into a number of smaller meshes. A fast technique that optimises the calculation of the Jacobian matrix values for multi-channel systems was also developed. A 1-D wavelet transform method was then used to compress the storage of the Jacobian matrix, in turn reducing the computer time and memory required to solve the least-squares optimisation equation to determine the inverse model resistivity values. The new techniques reduce the calculation time and memory required by more than 80% while producing models that differ by less than 1% from that obtained using the standard inversion technique with a single mesh. We present results using a synthetic model and a field data set that illustrates the effectiveness of the proposed techniques.

Data Availability Statement

The data that support the findings of this study are available from the corresponding author upon reasonable request.

INTRODUCTION

3-D ERT (Electrical Resistivity Tomography) surveys are now widely used to map areas with complex geology (Loke *et al.* 2013a). Most surveys use multi-channel resistivity meter systems with the electrodes planted in the ground. A system with 32 to 128 electrodes linked by multi-core cables to the resistivity meter is frequently used. The number of unique electrode positions used in the survey usually does not exceed a few thousand. Compared to normal 'static' resistivity meter systems, 'mobile' systems use a cable with a more limited number of electrodes (4 to 12) that is pulled along the surface. Some surveys use a normal galvanic resistivity-meter system with a streamer pulled behind a boat in a water-covered area (Rucker and Noonan 2013; Simyrdanis *et al.* 2015). In land surveys capacitively coupled systems (Hildes *et al.* 2005; Kuras *et al.* 2006; Unrau 2019) can be used that avoid direct galvanic contact with the ground where a limited number of measurements are simultaneously made at approximately regular intervals. Both types use a GPS receiver attached to a computerised central system to trace the position of the line and subsequently estimate the actual position of the electrodes with a certain accuracy based on specific assumptions (Oikonomou *et al.* 2019). The streamer is pulled to and fro crisscrossing the survey area to get dense data coverage. In some surveys, the number of unique electrode positions can exceed a hundred thousand. A 3-D finite-element mesh is used to model the resistivity data so that topography can be directly incorporated into the inverse model (Loke 2000). To accurately model the data from such large surveys, a dense mesh with more than one million nodes is sometimes used. The combination of a large number of electrode positions together with a large mesh presents computational problems in terms of computer execution time and high memory demands.

To reduce these computational issues, some researchers in the past have resorted to shortcuts, such as binning electrode positions, nudging electrode positions and subdomains. Xu and Dunbar (2015) took methods from marine-based streaming seismic acquisition through data binning. The technique of binning converts a series of closely spaced 2-D profiles into a quasi-3-D survey through combining scattered data points onto regular grids and then conducting 3-D inversion. The survey is divided into multiple rectangular horizontal zones called bins on the surface and each measurement is assigned to a bin according to the midpoint between the source and the receiver. The apparent resistivity measurements are sorted into bins based on the centre points of each four-electrode configuration and there will typically be multiple measurements placed into a single bin. The bin size is selected based on the data density and the required resolution of the 3-D inversion, balanced with the time required to complete the resulting 3-D inversion. Rucker *et al.* (2009) used a concept called nudging to move the electrode positions for ease of modelling. To decrease the number of unique electrode positions, thereby reducing the number of mesh nodes needed for inversion, they nudged electrodes to the nearest 3 m. The initial survey design was established on a 3 m grid, but a few of the electrode coordinates for non-orthogonal lines had to be repositioned to reduce memory storage. Their justification for nudging was a trade-off between accuracy and expediency, for what was at the time, the largest published 3-D modelling study with over 7,000 electrode positions.

Rucker *et al.* (2009) also experimented with manually dividing the large model domain into individually processed, smaller subdomains in order to reduce the computer memory

usage; computer memory was generally quite low at the time of the study relative to today. Experiments with the subdomains included increasing the amount of overlap for adjacent models. Four sets of model overlap were tested including: 15 m (6 total model domains), 50 m (8 total model domains), 100 m (15 total model domains), and 150 m (50 total model domains). The results of modelling with a large number of subdomains were undesirable, showing mismatches in target shape and values in the areas of overlap.

In this paper we describe techniques to reduce the computer time and memory needed so that the data inversion to produce a 3-D model can be completed within a reasonable time with common personal computers. We use a method similar to Rucker *et al.* (2009) in creating subdomains. Here, we refer to it as mesh segmentation. The difference in the methodology, however, is that the overlap from one domain is accommodated in the other domains to ensure continuity in model values. While the potentials and sensitivity values are calculated individually for each segment (similar to the subdomain technique), a single unified model inversion step is carried out that covers the entire survey area. This greatly reduces mismatches in the areas of overlap.

We test the new mesh segmentation method on synthetic and field data sets and demonstrate that the results are nearly identical to modelling all of the data using a single mesh. The advantage, however, is the significantly reduced computer time and memory.

DATA INVERSION METHOD

For 3-D ERT data sets, the smoothness-constrained least-squares optimisation method is widely used (Li and Oldenburg 2000, Loke *et al.* 2013a). The linearised least-squares equation that gives the relationship between the model parameters (\mathbf{r}) and the data misfit (\mathbf{g}) is given below.

$$[\mathbf{J}_i^T \mathbf{R}_d \mathbf{J}_i + \lambda_i \mathbf{W}^T \mathbf{R}_m \mathbf{W}] \Delta \mathbf{r}_i = \mathbf{J}_i^T \mathbf{R}_d \mathbf{g}_i - \lambda_i \mathbf{W}^T \mathbf{R}_m \mathbf{W} (\mathbf{r}_{i-1} - \mathbf{r}_m) \quad (1)$$

The Jacobian matrix \mathbf{J} contains the partial derivatives of the measured data (apparent resistivities) with respect to the model resistivity. The inversion procedure is stabilised through the roughness filter \mathbf{W} (deGroot-Hedlin and Constable 1990) with a damping factor λ . $\Delta \mathbf{r}_i$ is the required change in the model parameters (the logarithms of the model resistivity values) to reduce the data misfit \mathbf{g} while \mathbf{r}_{i-1} is the resistivity model from the previous iteration. The vector \mathbf{r}_m is a reference background model. \mathbf{R}_d and \mathbf{R}_m are weighting matrices used by the L1-norm inversion method (Farquharson and Oldenburg 1998) applied to the data misfit and model roughness. The inversion algorithm usually takes 3 to 6 iterations to converge. In the tests with the data sets carried out in this paper, we used the L1-norm for both the data misfit and model roughness. Further details on the practical use of the least-squares iterative method, such as the use of different norms and selection of the damping factor, can be found in the references (Farquharson and Oldenburg 1998; Loke *et al.* 2003; Farquharson and Oldenburg 2004; Loke *et al.* 2014a).

Each iteration requires the calculation of the model response (calculated apparent resistivity values) using the finite-element method and the Jacobian matrix using the adjoint-equation method (McGillivray and Oldenburg 1990). The least-squares equation (1) then needs

to be solved to determine the change in the model parameters ($\Delta \mathbf{r}_i$) to reduce the data misfit. The calculation time increases non-linearly with the finite-element mesh size and the number of data points and model parameters. In surveys using a mobile measuring system where the electrodes are on a streamer, the number of electrode positions, data points and model parameters can exceed more than a hundred thousand and the finite-element mesh used might have more than one million nodes. The calculation of the apparent resistivity and Jacobian matrix for each iteration can exceed a day on inexpensive PCs used by small companies and institutions. The complete inversion of a data set might take more than a week using standard techniques. To reduce the calculation time, we use a ‘divide and conquer’ strategy that subdivides the mesh in a number of smaller meshes (Christiansen and Auken 2004; Loke and Lane 2004).

Another computational problem is the size of the Jacobian matrix \mathbf{J} and the time taken to solve the least-squares equation (1). The \mathbf{J} matrix has n times m array elements, where n is the number of data points and m is the number of model parameters. As an example, a data set with 200,000 data points and a model with 150,000 model cells will have a Jacobian matrix with 30,000,000,000 array values. To solve the least-squares equation for such large matrices, the linear conjugate-gradient method together with a data compression technique (using wavelet transforms) is commonly used (Li and Oldenburg 2003; Davis and Li 2013). The inverse models used in this research have a simple arrangement with the model cells arranged in a 3-D rectangular pattern. We describe a simple technique to optimise the wavelet transform method for the model structure used in this research.

METHODS TO REDUCE COMPUTER TIME AND MEMORY

In this section, we described various methods used to reduce the computer time and memory required for the inversion of very large data sets with hundreds of thousands of electrode positions and data points. The calculations were carried out using a PC with an 18-core Intel W-2195 CPU and 256 GB of RAM.

Mesh segmentation

Surveys conducted with a mobile resistivity meter system are characterised by arrays having a limited footprint that is proportional to the length of the streamer. Figure 1 shows a schematic diagram of a streamer cable for a 10-channel resistivity meter system using a dipole-dipole arrangement. If the unit electrode spacing is 1 m, the furthest distance between a current and potential electrode is 12 m. The footprint of the system (Tsourlos *et al.* 2014) can be much smaller than the survey area which might be several hundred meters in length. Unlike a survey with a static resistivity meter system, where an array can have electrodes that extend across the entire survey line, the region of the subsurface that affects a measurement using a cable of limited length has a more limited lateral extent compared to the total length of the survey line. This property was previously used (Christiansen and Auken 2004; Loke and Lane 2004; Tsourlos *et al.* 2014) to reduce the calculation time for the inversion of data from long 2-D survey lines. We note that in some surveys a larger spacing might be used between the potential electrodes towards the end of the streamer (such as between electrodes P9 to P11 in Figure 1)

to obtain a stronger signal strength. However, the footprint of the system is still limited by the maximum length of the cable. We extend the segmentation technique to 3-D surveys.

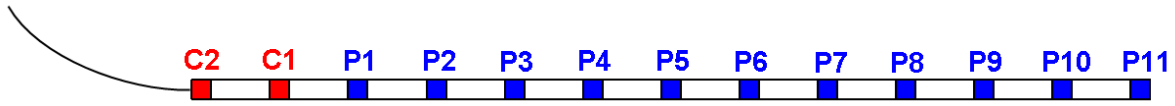


Figure 1. Schematic diagram of a mobile streamer. C1 and C2 are the current electrodes while P1 to P11 are the potential electrodes.

As an example, Figure 2 shows the algorithm used to subdivide a rectangular model grid with 160 by 45 cells in the x and y directions. In the first step (Figure 2a), the model grid is subdivided in 6 approximately equal segments. Next, we mark the data points with at least one electrode in segment 1. The electrode arrays near the boundaries of the segment are likely to have one or more electrodes outside the segment. The boundaries of the segment are next extended (Figure 2b) so that it covers all the electrodes that are used by data points marked earlier. In this example, the measurements are only made in the x direction, so only the x boundary is extended. In surveys with measurements in the y direction, the y boundary is similarly extended. In the final step, the boundaries in both the x and y directions are extended by 5 model grid lines (Figure 2c) so that the effect of model cells near edges of the segment are included in the calculation of the apparent resistivity and Jacobian matrix values for the data points that were marked for this segment. Next, the same procedure is used for segment 2 (Figure 2a). The data points that were marked for segment 1 are removed from the data set used for determining the data points that fall within segment 2 (as well as other segments). Next the boundaries for the remaining segments are set one by one using the same procedure. Note this procedure allocates a data point to only one segment in the calculation of the apparent resistivity and Jacobian matrix values. Figure 3a shows the final boundaries of the 6 segments. There is an overlap of 10 model grid lines at the boundaries of the neighbouring segments. The overlap minimises discontinuities in the calculated apparent resistivity and Jacobian matrix values near the boundaries.

To avoid the build-up of artefacts near the edges of the segments, the boundaries of the segments are changed after each iteration. In the second iteration of the least-squares optimisation method (Figure 3b), the boundaries for segment 1 are pushed forward in the x and y directions by 3 model grid lines. At the same time, the lower y boundary for segment 2 is pushed upwards in the y direction by 3 model grid lines. In the same way, the left x boundary for segment 3 is moved to the right by 3 model grid lines. In the third iteration (Figure 3c), the boundaries for segment 1 are pushed backwards in the x and y directions by 3 model grid lines from the positions in the first iteration. In the fourth iteration, the boundaries in the first iteration are used. The algorithm uses the alternating positions of the boundaries in a cyclic manner.

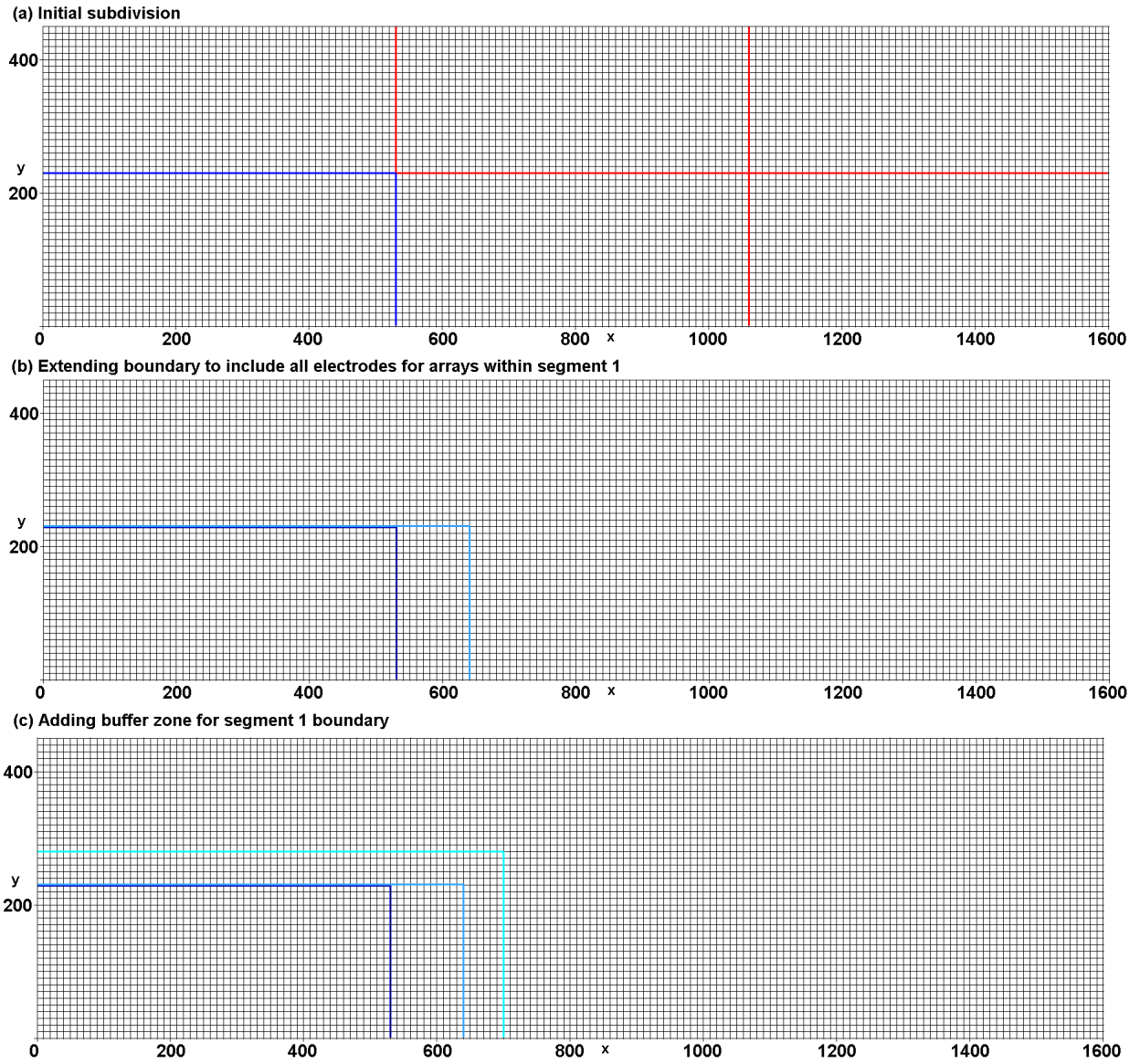


Figure 2. Method used to subdivide a model with 160 by 45 cells (of 10 m width in the x and y directions) in each layer subdivided into 6 segments. (a) Initial subdivision into 6 segments of approximately equal size. The dark blue line marks the region covered by segment 1. (b) Extending the boundary (medium blue line) of segment 1 so that it includes all the electrodes for data points in this segment. (c) Adding a buffer zone around the segment to minimise edge effects. The final region covered by segment 1 is shown by the light blue line.

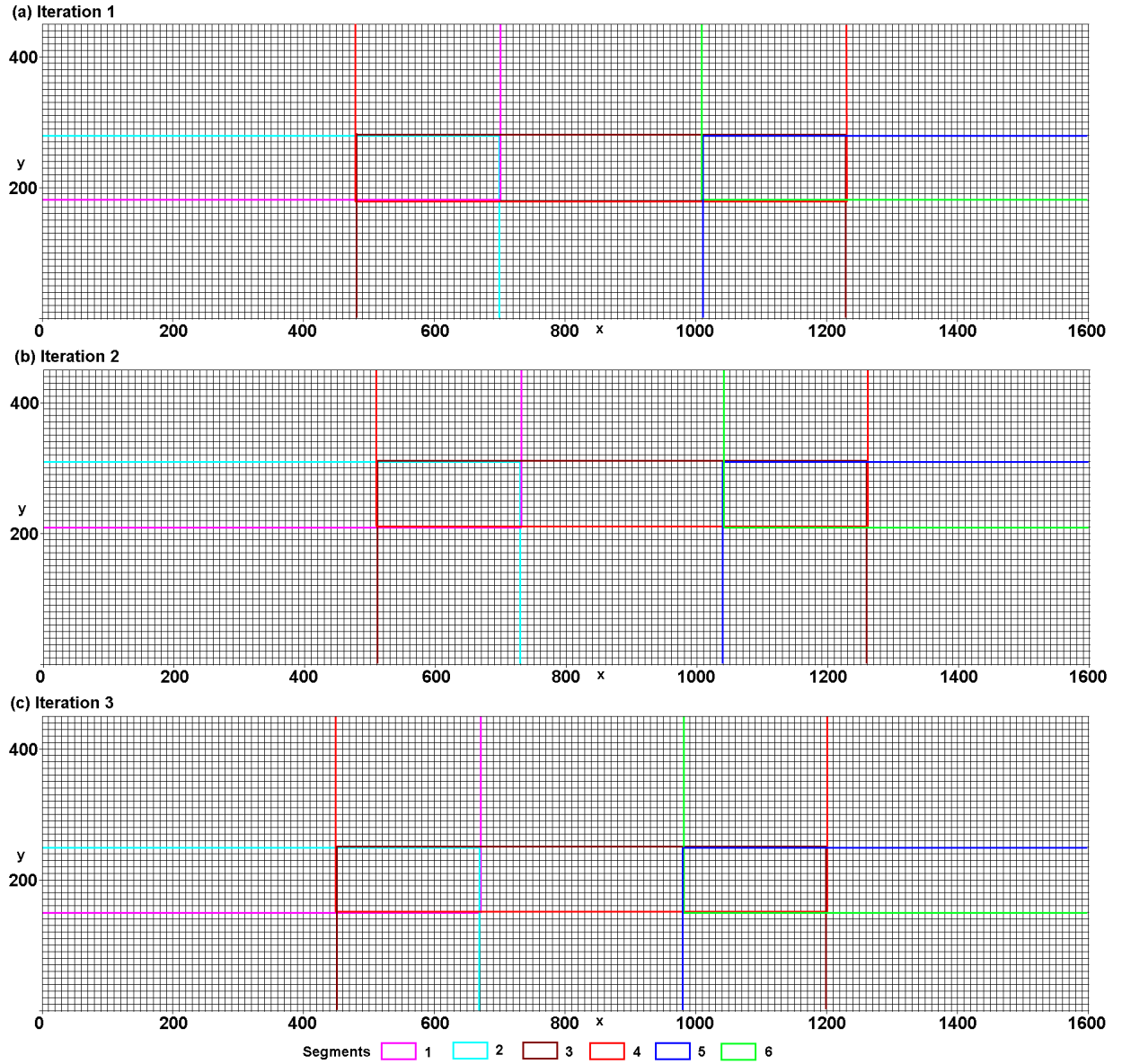


Figure 3. (a) The initial regions of the model grid covered by the 6 segments used in iteration 1 of the least-squares optimisation algorithm. Note the overlaps between neighbouring segments. (b) Shifting of the boundaries of the segments forwards by 3 model grid lines (compared to those used in iteration 1) in iteration 2. (c) Shifting of the boundaries of the segments backwards by 3 model grid lines (compared to those used in iteration 1) in iteration 3.

The segmentation algorithm extends the final boundaries of the segments by at least 5 model grid lines. The widths of the model cells are usually set to be the same as the minimum distance between adjacent electrodes in the streamer. Extending the boundaries to a larger distance should increase the accuracy of the model obtained by the segmentation method (compared to a normal single mesh inversion) but at the cost of larger computer memory and time. To estimate the optimum distance to extend the boundary, we first examine the sensitivity values for a dipole-dipole array survey similar to that used in the synthetic model and field survey discussed in this paper. Figure 4a shows a 3-D plot of the sensitivity values (Fréchet derivative) for a dipole-dipole array with $a=1$ m and $n=10$ for a homogeneous medium that can

be calculated analytically (Loke and Barker 1996). The regions with the highest sensitivity values are located near the electrodes. The isosurface plot shows the regions with significant sensitivity values are located near the dipoles and elongated in the direction perpendicular to the axis of the array. Figure 4a shows the model sensitivity distribution for a single array. To study the characteristics of a data set that consists of many arrays, the model resolution is used (Loke *et al.* 2014b). The resolution value of a model cell is limited to between 0.0 (no resolution) to 1.0 (perfect resolution). We calculate the resolution values for a data set from a survey grid with 64 by 23 electrodes (Figure 4b), with all the possible dipole-dipole measurements with $a=1$ m and $n=1$ to 10 in the x -direction only (giving a total of 12995 data points). The survey grid and number of electrodes is similar to a single segment in Figure 2. Figure 4b shows a 3-D plot of the resolution values. The subsurface is divided into uniform cells with dimensions of $1.0 \times 1.0 \times 0.5$ m. The maximum resolution value at the surface near the centre of the survey grid is about 0.84. The resolution values gradually decrease with increasing distance from the edge of the survey grid. The band with significant resolution values is wider at the y boundaries compared to the x boundaries. This is because the measurements are only made in the x direction, and the zone with higher sensitivity values are elongated in the direction perpendicular to the array axis. Figure 4c shows the change in the resolution values at the x and y boundaries with distance from the boundaries. For the y boundary, the cell at the surface immediately next to the boundary has significant resolution value of 0.76. The resolution rapidly decreases with distance to about 0.002 at 4.5 m. So, extending the segment boundary up to 5 times the unit electrode spacing should include all the regions with significant resolution values. Figure 4c also shows that the resolution values are lower at the x boundary, and also decreases with depth. Field data sets sometimes have measurements in both directions, so the boundary is normally extended by the same distance in both directions. Most conventional arrays have sensitivity patterns that do not extend as far out as the dipole-dipole array (Loke *et al.* 2014b). So, extending the segment boundaries to about 5 times the unit electrode spacing is a conservative approach that should cover most field surveys situations.

The time and taken by the finite-element method increases nonlinearly with the number of nodes in the mesh (Christiansen and Auken 2004; Loke and Lane 2004). Calculating the apparent resistivity values for all the data points using a number of smaller sub-meshes takes less time than using a single large mesh for very large models that might have more than a million nodes. Another benefit of using segments is the reduction in the calculation of the Jacobian matrix values. In the standard monolithic inversion approach, the sensitivity values for all the model cells are calculated for each data point. In the segmented inversion approach, the sensitivity values for only the model cells that fall within the segment are calculated for each data point. The average number of model cells in a segment for the grid in Figure 3a is 14960 which is about 26% of the entire model with 57600 cells (with 10 layers). For larger model grids, with grid sizes much larger than the overlap between adjacent segments, the Jacobian matrix calculation time is usually reduced to about 20% compared to the standard single mesh inversion method.

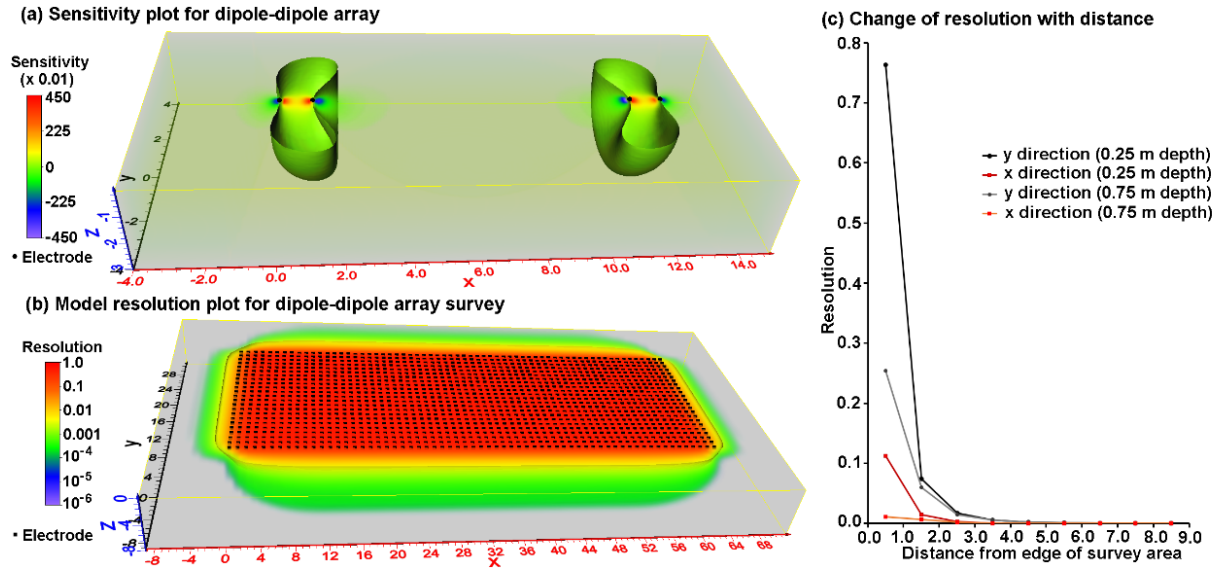


Figure 4. (a) 3-D plot of sensitivity values for the dipole-dipole array with $a=1$ m and $n=10$. The electrodes are located at x positions of 0, 1, 11 and 12 along the $y=0$ axis. The isosurface for sensitivity value of 0.01 is shown. (b) Plot of resolution values for a dipole-dipole array survey with $a=1$ m and $n=1$ to 10 with electrodes in a 64 by 23 grid. The 0.005 isosurface is shown. The electrodes are marked by black dots on the surface. (c) Change of resolution with distance from edge of survey grid at the x and y boundaries. The resolution values of cells at the mid-point of the x and y boundaries (which have the highest values) are shown.

Optimising the Jacobian matrix computations for multi-channel systems

The Jacobian matrix is frequently calculated using the adjoint-equation method for resistivity problems (Sasaki 1989; McGillivray and Oldenburg 1990). Many modern resistivity meter systems have multi-channel capability where a number of simultaneous potential measurements are made for a single injection of the current. As an example, the arrangement in Figure 1 makes 10 measurements using the same C1-C2 current dipole. This feature can be used to reduce the numerical calculations required by the adjoint-equation method to calculate the sensitivity values for the 10 data points that share the same current electrodes positions. The finite-element method is commonly used to calculate the apparent resistivity values for surveys over areas with topography (Loke 2000). The potentials are calculated by solving the following capacitance matrix equation (Sasaki 1989; Silvester and Ferrari 1990; Loke *et al.* 2018).

$$\mathbf{C}\Phi = \mathbf{s} \quad (2)$$

Φ is a vector that contains the potentials at the nodes of the finite-element grid while \mathbf{s} is the current source vector. \mathbf{C} is the capacitance matrix that contains the positions of the nodes and the model conductivity values. Figures 5a and 5c show the quadrilateral and hexahedral elements used for 2-D and 3-D models. For the following discussion, we use the 2-D mesh (Figure 5b) as an example as the matrix structure (Figure 5d) is easier to visualise. However, the matrix equations for both the 2-D and 3-D finite-element methods are essentially the same.

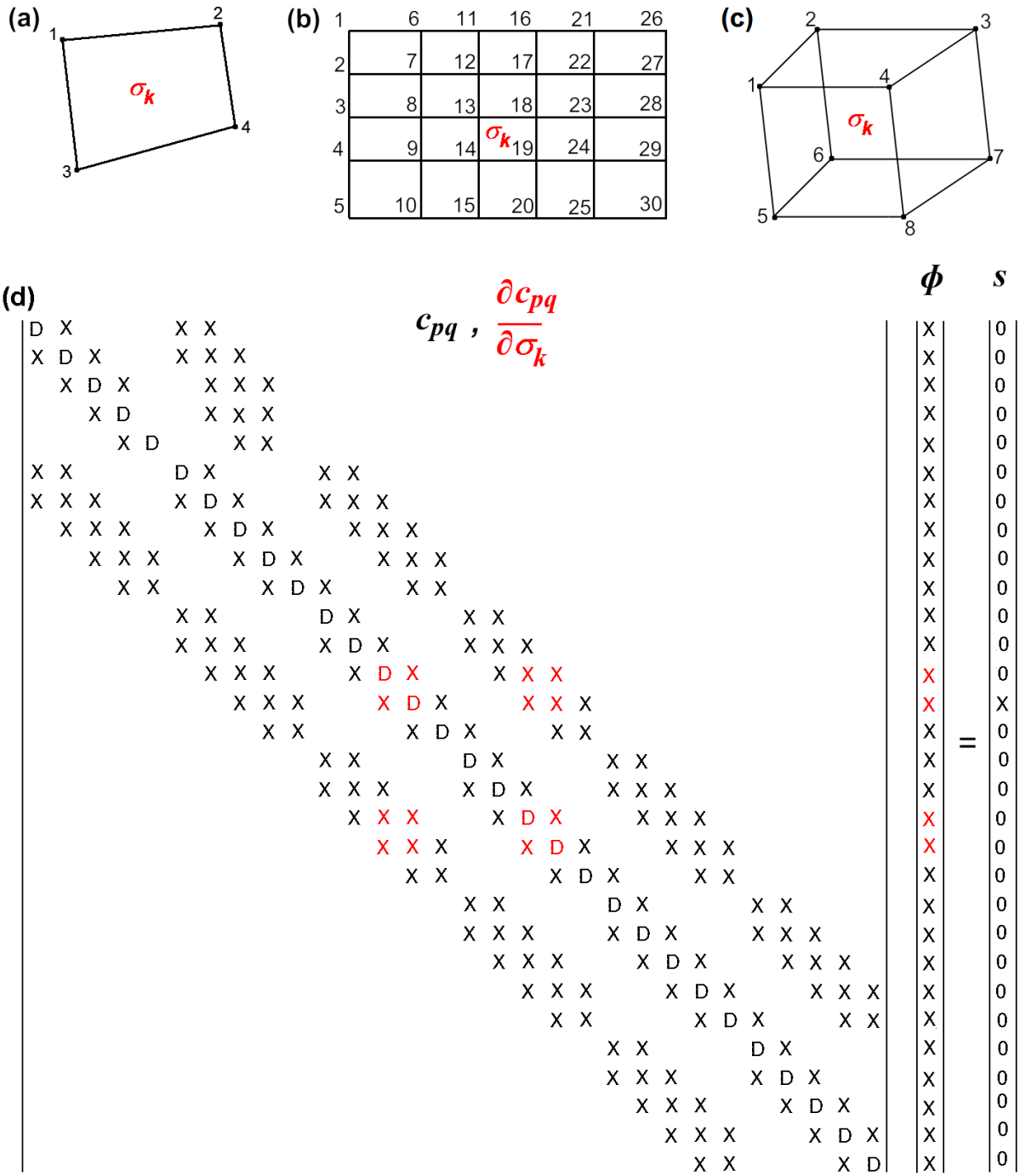


Figure 5. (a) 2-D quadrilateral element with 4 nodes. (b) Example 2-D finite-element mesh with node numbers. (c) 3-D hexahedral element with 8 nodes. (d) Schematic diagram of the structure of the capacitance matrix equation for the 2-D mesh with the non-zero elements. D represents a diagonal element while X represents a non-zero off-diagonal element. The members of the $\frac{\partial \mathbf{C}}{\partial \sigma_k}$ matrix (due to a change in the conductivity of the k mesh cell) that have non-zero values are marked in red.

Differentiating the capacitance matrix equation (2) with respect to the model cell conductivity σ_k leads to the following relationship.

$$\mathbf{C} \frac{\partial \Phi}{\partial \sigma_k} = - \frac{\partial \mathbf{C}}{\partial \sigma_k} \Phi \quad (3)$$

This equation has the same form as equation (2). All the information required to calculate the sensitivity $\frac{\partial \Phi}{\partial \sigma_k}$ is available in the process of solving equation (2) to calculate the potentials. The matrix $\frac{\partial \mathbf{C}}{\partial \sigma_k}$ is very sparse with only 16 non-zero terms for a 2-D trapezoidal element (Figure 5d). The terms in the capacitance matrix \mathbf{C} consists of the coupling coefficients between the nodes in each element in the mesh (Silvester and Ferrari 1990) and the conductivity of the element. The coupling coefficient between two nodes in an element (Figure 5a) has the following form.

$$c_{pq} = d_{pq}(x, z) \sigma_k \quad (4)$$

The function $d_{pq}(x, z)$ depends only on the coordinates of the four nodes at the corners of the trapezoidal element. The derivative of the coupling coefficient with respect to the element conductivity is thus given by

$$\frac{\partial c_{pq}}{\partial \sigma_k} = d_{pq}(x, z). \quad (5)$$

As the $d_{pq}(x, z)$ terms are calculated in the process of constructing the capacitance matrix \mathbf{C} in equation (2), so it is not necessary to recalculate them for the $\frac{\partial \mathbf{C}}{\partial \sigma_k}$ matrix. In terms of computer

program implementation, calculating a member of the $\frac{\partial \Phi}{\partial \sigma_k}$ vector, basically involves the multiplication of a 4 by 4 non-zero sub-matrix (containing the d_{pq} terms for the mesh element) by the potentials (Φ) at the nodes due to current sources located at the positions of the current electrodes used in the measurement (Figure 5d). This is represented by the following equation.

$$\mathbf{e} = \frac{\partial \mathbf{C}}{\partial \sigma_k} \Phi \quad (6)$$

This produces a vector (\mathbf{e}) with 4 non-zero values that is in turn multiplied by the potentials at the nodes due to current sources located at the positions of the potential electrodes. The calculation of the \mathbf{e} vector requires 16 multiply-add operations for a 2-D quadrilateral element. In total 20 multiply-add operations are required for each mesh element.

For a 3-D hexahedral element, calculating the \mathbf{e} vector involves the multiplication of an 8 by 8 non-zero sub-matrix with a vector which requires 64 multiply-add operations. It is then followed by 8 multiply-add operations to add the potentials at the 8 nodes of the element due to current sources at the potential electrodes giving a total of 72 multiply-add operations. We note that for both the 2-D and 3-D problems, the most time-consuming part is in the calculation of the \mathbf{e} vector in equation (6).

However, the \mathbf{e} vector only involves the current electrodes and is independent of the position of the potential electrodes used in a measurement. If there is a series of measurements

that use the same positions of the current electrodes, it is only necessary to calculate the \mathbf{e} vector once and store the values in a temporary array in the computer memory. The temporary array is then used to calculate the Jacobian matrix values for subsequent measurements that use the same current electrodes. As an example, the electrodes arrangement in Figure 1 uses the same C1-C2 current dipole for 10 different measurements. Thus, it is only necessary to directly calculate the \mathbf{e} vector for the first measurement that uses the C1-C2-P1-P2 electrodes. For the 9 subsequent data points (using the C1-C2-P2-P3 until C1-C2-P10-P11 configurations) it is not necessary to directly calculate the \mathbf{e} vector which can be retrieved from the computer memory. This means that while the calculation of the sensitivity value for the first measurement requires 72 multiply-add operations, the sensitivity values for the 9 subsequent measurements require only 8 multiply-add operations each. This reduces the total number of multiply-add operations for the 10 data points from 720 to 144 which reduces the calculation time by about 80% for 3-D problems.

It was noted by Loke *et al.* (2015) in the study of optimised arrays that for some data sets the number of independent current-potential (C-P) pairs can be much less than the number of data points. This was used to greatly reduce the calculation time to generate the optimised arrays. The same technique can be used to further reduce the calculation time for the Jacobian matrix for data sets where the number of unique C-P pairs is much less than the number of data points. However, the benefit of using this technique is highly data dependent. For surveys that use the same current electrodes for a large number of data points (Blome *et al.* 2011) using a resistivity meter with a large number of channels this can be highly beneficial. For some data sets, such as those using the Wenner array or the Lambayanna field data set (following section), it can be slower. The expected reduction (or increase) in computer time using this technique can be estimated by calculating the number of unique C-P pairs versus the number of data points.

These techniques to reduce the Jacobian matrix calculation time for parallel measurements are general in nature and can also be used for standard inversion using a single mesh, as well as for other geophysical methods such as EM surveys that use a number of receivers for a single source position.

The calculation of the Jacobian matrix requires the largest amount of computer memory during the inversion process. If the number of electrodes used in the survey is n_e and the number of nodes in the mesh is n_m , the total number of potential values is $n_e \cdot n_m$. The synthetic model example used in this paper (following section) has 7406 electrodes and the finite-element mesh has 811,980 nodes. If the potentials are stored as 4-byte single precision values, the computer memory needed to store all the potential values is 22.4 GB. If the mesh is divided into 6 segments, the average number of electrodes and nodes in a segment are 1,418 and 267,320 respectively. Thus, the average amount of computer memory required by the segmentation method is about 1.4 GB which is 6.3% of that used by the standard monolithic approach. If the computer memory available is less than that required, it is still possible to calculate the Jacobian values by reading the potential values associated with the 4 electrodes used for each data point from the computer hard-disk when required. However, this is much slower than loading all the potential values into the computer memory where they can be accessed more rapidly.

Reducing the computer time and memory to solve the least-squares equation

The Jacobian matrix \mathbf{J} encountered for large surveys with hundreds of thousands of data points and model cells can have billions of array values. For such large scale problems, the iterative linear conjugate-gradient method is commonly used to solve the least-squares equation (1) to determine the change in the model parameters $\Delta \mathbf{r}_j$. Solving the least-squares equation using the linear conjugate gradient method involves matrix vector multiplications of the form $\mathbf{J}^T \mathbf{a}$ and $\mathbf{J} \mathbf{b}$. The size of the Jacobian matrix presents two computational problems. The first involves the computer time required for the matrix-vector multiplications. The second problem is that the size of the Jacobian matrix might exceed the computer memory. Both problems were solved by using the wavelet transform to compress the Jacobian matrix by retaining only the components with significant amplitudes (Li and Oldenburg 2003; Davis and Li 2013). The arrangement of model cells used in this research has a simple 3-D rectangular pattern (Figure 5) so a simple algorithm can be used to optimise the use of the wavelet transform. The sensitivity values associated with an electrode measurement configuration is a 3-D function of the (x, y, z) coordinates of the model cells. We take advantage of the regular arrangement of the model cells, and the property that sensitivity values change in a smooth manner between neighbouring cells, to convert the 3-D sensitivity function to a 1-D function of the cell index number (Figure 6) so that a simple 1-D wavelet transform can be used. As an example, Figure 7a shows the Jacobian vector for a single pole-dipole array on the surface of a model with a 15 by 15 m rectangular grid and 7 layers plotted as a 1-D function of the cell index number. The Jacobian vector has the largest amplitudes at the model cells that are closest to the electrodes, with the amplitudes decreasing with each deeper layer. The shift in the position of the sensitivity pattern between layers is due to the zigzag model cell numbering scheme used (Figure 6). The fast wavelet transform using the Daubechies 4 wavelet (Daubechies 1988; Press *et al.* 2007) was used to calculate the wavelet components (Appendix). The wavelet components plot (Figure 7d) shows that most of them have very small amplitudes. If components with amplitudes of less than 0.5% of the largest are removed, the reconstructed sensitivity (using the inverse wavelet transform) plot still closely matches the original plot (Figures 7a and 7b). Figure 7c shows a plot of the difference between the original and reconstructed Jacobian values. Note the vertical scale used for this plot is 100 times smaller compared to Figures 7a and 7b. If the same scale is used, the plot will appear as a flat line. The maximum amplitude of the difference is about 200 times smaller (or 0.5%) than the maximum Jacobian value.

For very large models with hundreds of thousands of model cells, the 1-D wavelet transform reduces the size of the Jacobian matrix by more than 100 times. As an example, the Jacobian matrix for the Lambayanna field data set (following section) has 69,464,915,000 elements, or about 259 GB of computer memory (using a 4-byte single precision array) which exceeds the memory of the PC used. This was reduced to 139,579,108 values if only the wavelet components with amplitudes that exceed 0.5% of the maximum amplitude are retained. This is nearly 500 times smaller than the full Jacobian matrix. The computer memory required is slightly over 1 GB (including an auxiliary 4-byte integer array with the index values of the retained wavelet components). The time taken by the fast wavelet transform and to solve the

least-squares equation using the sparse transformed Jacobian matrix is less than 10% of the time taken by the finite-element routine to calculate the potentials and Jacobian matrix values.

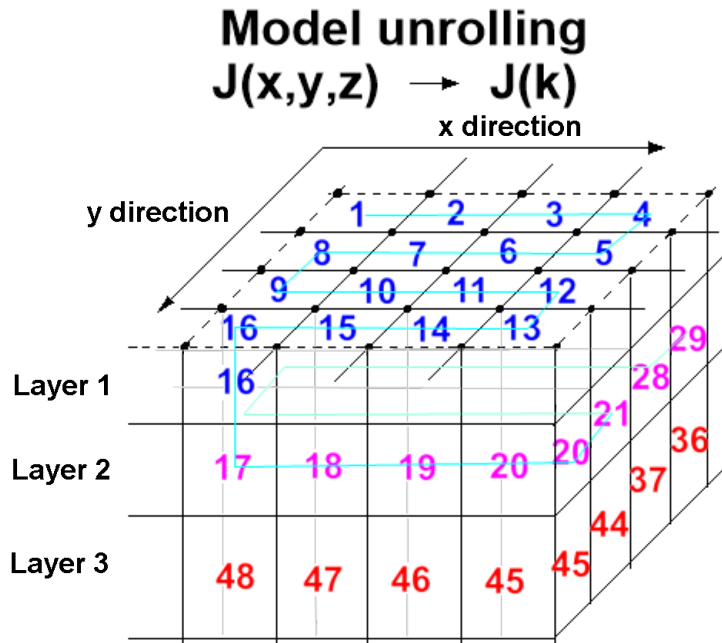


Figure 6. Numbering of model cells arranged in a 3-D rectangular grid so that the Jacobian matrix which is a 3-D function of (x,y,z) is converted to a continuous 1-D function of the model cell index k .

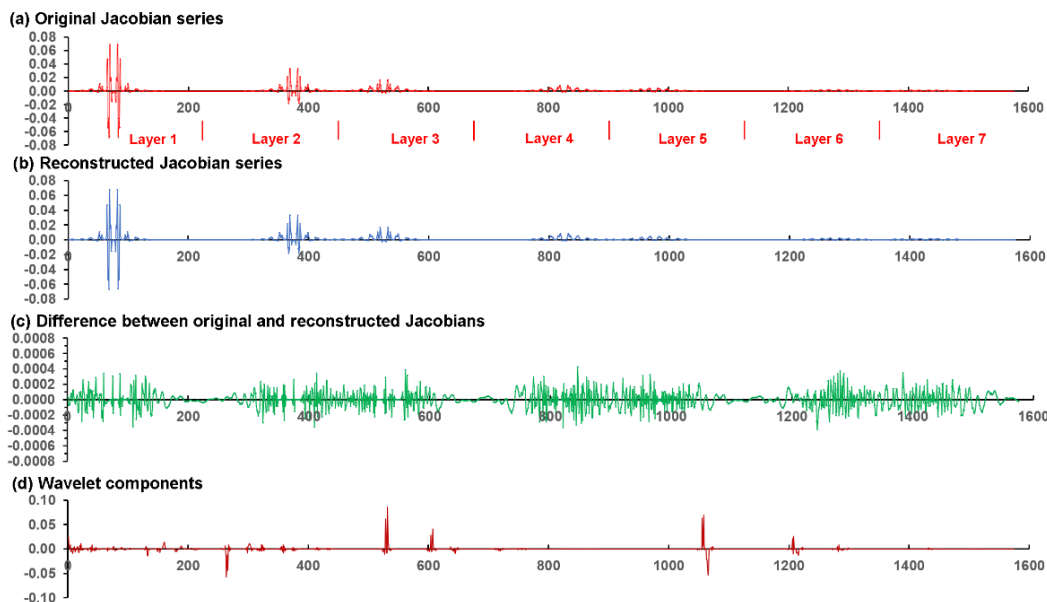


Figure 7. (a) Plot of the Jacobian values for a single pole-dipole array ($a=2, n=1$) for a model with $15 \times 15 \times 7$ model cells (each layer has 225 cells). (b) The reconstructed Jacobian values after wavelet components with amplitudes of less than 0.5% of the maximum value were removed. (c) Plot of the difference between the original and reconstructed Jacobian values. Note the vertical scale is 100 times smaller than (a) and (b). (d) Plot of the wavelet components. Values in vertical axis in the plots are dimensionless while the horizontal axis is the model cell index number in (a), (b) and (c), and the wavelet wave number in (d).

For very large models with hundreds of thousands of model cells, the 1-D wavelet transform reduces the size of the Jacobian matrix by more than 100 times. As an example, the Jacobian matrix for the Lambayanna field data set (following section) has 69,464,915,000 elements, or about 259 GB of computer memory (using a 4-byte single precision array) which exceeds the memory of the PC used. This was reduced to 139,579,108 values if only the wavelet components with amplitudes that exceed 0.5% of the maximum amplitude are retained. This is nearly 500 times smaller than the full Jacobian matrix. The computer memory required is slightly over 1 GB (including an auxiliary 4-byte integer array with the index values of the retained wavelet components). The time taken by the fast wavelet transform and to solve the least-squares equation using the sparse transformed Jacobian matrix is less than 10% of the time taken by the finite-element routine to calculate the potentials and Jacobian matrix values.

RESULTS

Synthetic model test

We use a synthetic model with 8 blocks embedded in the upper layer of a two-layer medium (Figure 8). The electrodes are arranged in a 1610 by 460 m rectangular grid with a 10 m spacing in both the x and y directions for a total of 7,406 electrodes (Figure 2). The test data set consists of the dipole-dipole array measurements with the dipole length $a=10$ m, and dipole spacing values n of 1 to 10 with only measurements made in the x -direction. This gave a data set with 70,610 measurements while the inverse model with 10 layers has 57,600 cells. The main purpose of the synthetic data set is to check the accuracy of the segmentation inversion algorithm compared to the standard single mesh inversion. Gaussian random noise with an amplitude of 0.05 m Ω was added to the calculated resistance values (with a range of 0.54 to 355.18 m Ω) before they were converted to apparent resistivity values (Zhou and Dahlin 2003). This resulted in an average noise level of about 1.5% in the apparent resistivity values. The mesh was divided into 6 segments with the boundaries cutting across blocks 1, 3, 6, 7 and 8.

Figure 9a shows the inverse model using the standard inversion method with a single mesh that has a data misfit of 1.5%, which is the same as the added noise. The inverse model using the segmented mesh (Figure 9b) is nearly identical to that obtained with a single mesh and has the same data misfit. The edges of the segments were extended by 5 cells in both the x and y directions. In algorithms that do not calculate the Jacobian values for all model cells for each data point (Christiansen and Auken 2004; Loke and Lane 2004; Papadopoulos *et al.* 2011), the Jacobian values that are not directly calculated are normally set to zero in advance omitting their respective calculation. In this paper, we also test the results when the Jacobian values for these cells are approximated by using the values for a homogeneous half-space that can be calculated analytically (Loke and Barker 1996).

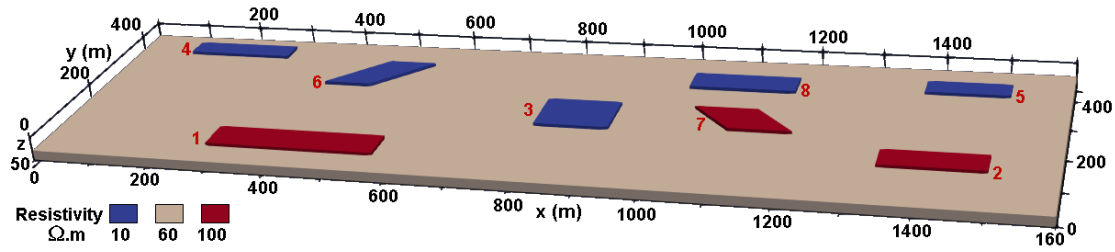


Figure 8. Synthetic model with 8 blocks in the upper layer of a two-layer medium. The top layer (transparent in the plot) has a resistivity of 30 $\Omega.m$ and a thickness of 23.2 m. Blocks 1 to 5 extend from the surface (0.0 m) to a depth of 5.0 m. The top of blocks 6 to 8 is at 5.0 m while the bottom is at 10.5 m depth.

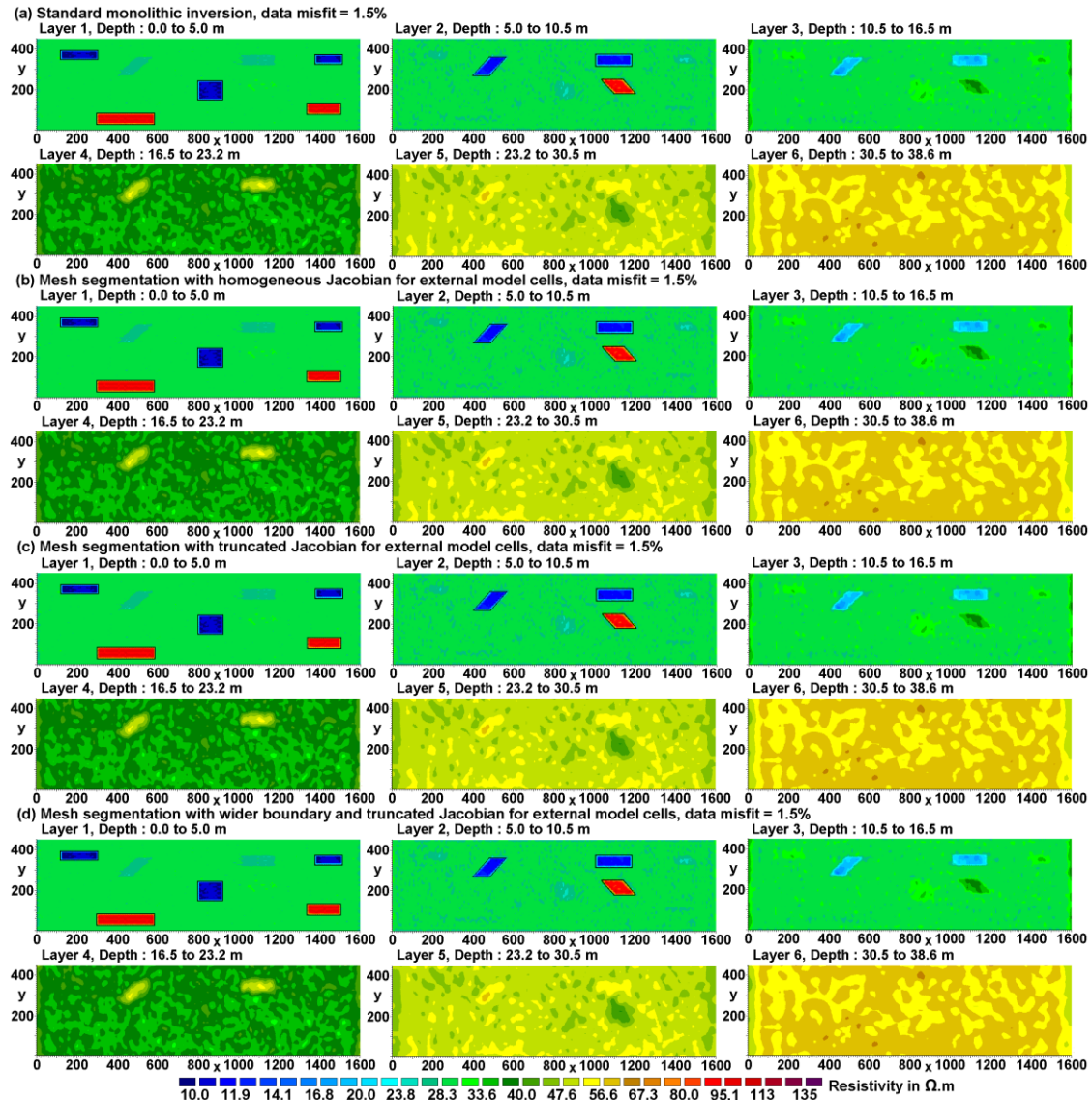


Figure 9. Inverse models of synthetic data set with (a) standard monolithic inversion, (b) using 6 segments with buffer zone of 5 model cells and homogeneous Jacobian approximation for external cells, (c) using segments with buffer zone of 5 model cells and truncated Jacobian for external cells and (d) using segments with buffer zone of 8 model cells and truncated Jacobian for external cells. The blocks in the synthetic model are shown by black outlines in the first 2 layers.

To numerically assess the accuracy of the segmented mesh model, the percentage relative difference at cell j between the resistivity of the models using standard monolithic (r_1) and segmented mesh (r_2) inversions was calculated using the following equation.

$$\partial(j) = 100 \cdot [r_2(j) - r_1(j)] / r_1(j) \quad (7)$$

The average percentage relative difference (∂_a) was then calculated using the following equation.

$$\partial_a = \left[\sum_1^m |\partial(j)| \right] / m \quad (8)$$

m is the number of model cells. The average difference between the model resistivity values obtained using the segmentation algorithm and normal monolithic inversion is 0.2% (Table 1). The maximum difference of 1.8% occurs in Layer 9 (not shown) which is probably due to the decrease in resolution with depth. There are no visible artefacts where the segment boundaries cut across the blocks in the upper layer. We also carried out an inversion with the fixed segment boundaries (instead of changing the boundaries after each iteration). The resulting model resistivity values also had an average difference of 0.2% but the maximum difference was higher at 2.4%.

Figure 9c shows the inverse model using the segmentation algorithm with the Jacobian values for the cells outside the segments truncated to zero. The average difference in the model values is essentially the same as for Figure 9b (to within 0.05%) but the maximum difference is slightly higher at 2.3%. For the final test, the width of the buffer zone at the edges of the segments was extended to 8 model cells with the Jacobian values outside the segments also truncated to zero (Figure 9d). This gave a maximum difference of 1.6% that is marginally lower (Table 1) compared to that obtained using a buffer zone of 5 model cells and a homogeneous model Jacobian approximation for the external cells.

We note that the models using the segmentation algorithm are visually identical to that obtained using standard monolithic inversion. The average difference of about 0.2% in the model resistivity values is small compared to the noise level of 1.5% added to the data. Padding the Jacobian matrix with approximate values from a homogeneous half-space does result in a slightly lower maximum difference when a narrower buffer zone is used. In cases where the approximate Jacobian is not suitable and the values are truncated to zero, using a wider buffer zone gave similar results at a cost of a slight increase in computer time (Table 1).

The different implementations of the segmentation algorithm reduce the calculation time by about 30% to 40% (Table 1). This is a relatively small data set with 7,406 electrodes, 70,610 data points and 57,600 model cells. There is a significant overlap between the different segments compared to the overall model grid size so the reduction in the computer time is relatively modest compared to larger data sets.

Table 1. Comparison of different methods for the inversion of the synthetic model data set. All the models have the same data misfit of 1.5%.

Inverse method	Inversion Time (s)	% model difference Average (max)	Memory required by adjoint-equation method (GB)
Single mesh	3,449		22.4
Segments with homogeneous Jacobian approximation for external model cells	2,140	0.2 (1.8)	1.4
Segments with truncated Jacobian for external model cells	2,025	0.2 (2.3)	1.4
Segments with wider buffer zone and truncated Jacobian for external model cells	2,512	0.2 (1.6)	1.6

Lambayanna field survey data set

Figure 10a shows the layout from a survey in a prehistoric submerged archaeological site in central Greece using a mobile streamer dragged along the sea bottom below the sea surface in a depth ranging from 0.9 m to 5.3 m and an average depth of 2.7 m (Oikonomou *et al.* 2019). The dipole-dipole array with dipole length $a = 1$ m and n values from 1 to 10 was used. There are 215,875 electrode positions and 164,414 data points in this data set. The survey lines, inverse model grid and segments used are shown in Figure 10b. Many of the survey lines crisscross each other such that several electrodes from different survey lines are located close to one another. In cases where the electrode does not coincide with a node in the finite-element mesh, an interpolation method is used (Spitzer *et al.* 1999; Loke *et al.* 2013b). The potential at the position of the electrode is estimated from the potentials at the four nearest nodes in the mesh (and similarly a current electrode is replaced by four equivalent current sources). The top 5 levels of the finite-element mesh are used to model the water layer where the resistivities of the cells are fixed using the measured seawater value of $0.17 \Omega\text{m}$ (Dahlin and Loke 2018). The z position of the 5th node from the top of the mesh is set at the measured depth of the seabed at the particular (x,y) position.

The model grid used for the data inversion has 131 by 326 cells with widths of 1 m in both the x and y directions and 10 layers giving a total of 422,500 model cells. The thickness of the first layer is set at the minimum depth of investigation (Edwards 1977) of the data set. The thickness of each deeper layer is increased by 15% since the data resolution decreases with depth. The maximum depth of investigation of the data set is used as a guide to set the depth to the bottom layer. Figure 11a shows the top 6 layers of the model with the standard monolithic inversion approach using a single finite-element mesh with 9,675,548 nodes. The mesh has 419, 1004 and 23 nodes respectively in the x , y and z directions. Out of the 23 nodes in the z direction, 5 nodes are used to model the water layer while 7 nodes are used for the bottom section of the mesh below the last model layer. The spacing between the 7 bottom mesh lines are progressively increased so that the last mesh line is sufficiently far away from the electrodes (Dey and Morrison 1979). The remaining 11 nodes are used for the 10 model layers with the top layer (which is closest to the electrodes) subdivided in two mesh lines. Figure 12 shows a 3-D plot of the model for the sediments below the water layer. As the water layer resistivity is

fixed, it is not shown in the model plots. The archaeological features of interest are represented by the higher resistivity anomalies on the left side of the sections (that is located further from the shoreline) in the top 3 layers. The inversion took about 327,777 seconds (91.0 hours). The data misfit of 10.8% is higher than most land surveys using a conventional ‘static’ multi-electrode resistivity meter system with the electrodes planted in the ground. This is probably partly due to the challenging marine environment with very conductive seawater and the continuous movement of the cable during the survey. Nevertheless, the resistivity model agrees with known archaeological information and the results from other geophysical surveys (Oikonomou *et al.* 2019).

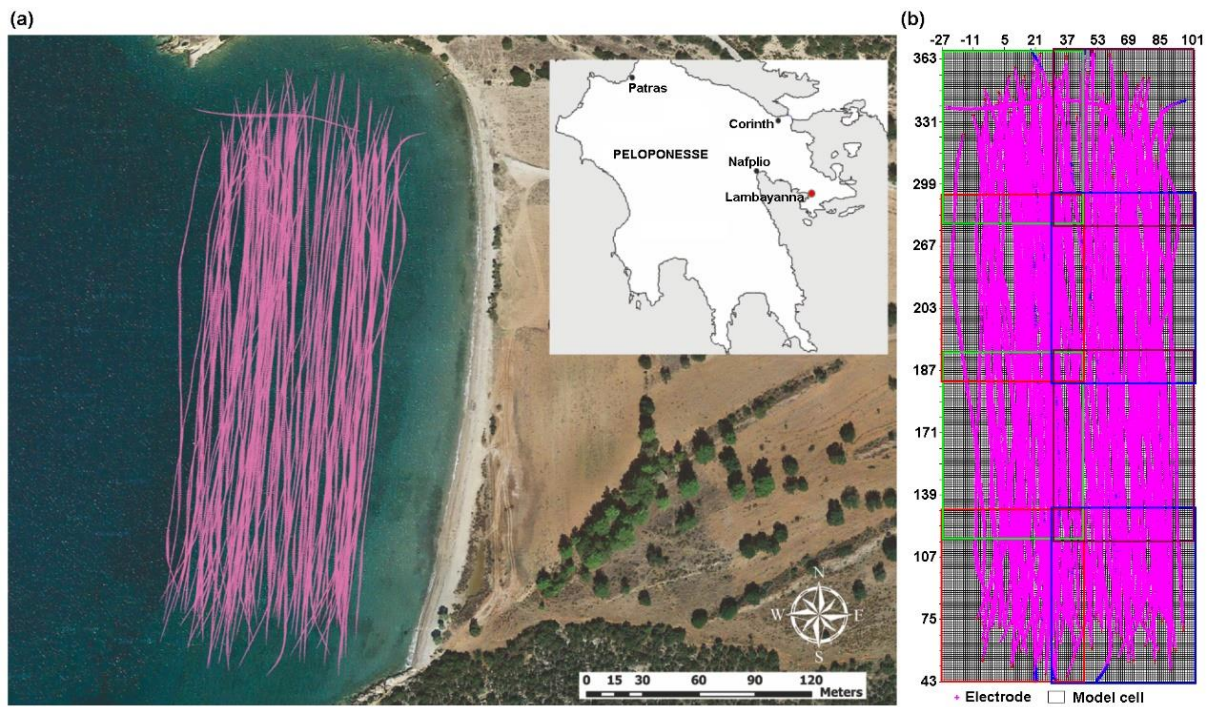


Figure 10. Lambayanna survey (a) map (survey location marked by red circle) and (b) inverse model grid (segments shown by coloured grid lines).

Figure 11b shows the model obtained using the segmentation algorithm with 8 segments. A buffer zone with 8 model cells was used for the segments. It was observed that the sensitivity values for model cells outside the segments calculated using the adjoint equation method (from the single mesh inversion) differ significantly from approximate values using a homogeneous model. This is probably because of the large contrast between the seawater and the subsurface materials. The Jacobian values for the cells outside the segments were thus truncated to zero in the inversion process, and a wider buffer zone was used for the segments. There are no significant differences in the models using the standard monolithic and segmentation inverse method (Figures 11a and 11b) that also has a data misfit of 10.8%. The average difference in the model resistivity values is 0.7%. The maximum difference of 3.9% occurred for a cell in the 9th layer which is probably due to the decrease in the resolution with depth. The calculation time was 52,731 seconds (14.6 hours), or a reduction of about 84% compared to the standard approach. The average number of model cells in a segment is 78,485 (about 19% of the whole model).

We also carry out a test with an alternative approach where the positions of the electrodes were rounded up (Oikonomou *et al.* 2019), or binned, to the nearest 0.5 m (i.e. half the electrode spacing). This reduced the number of electrode positions to 87,245 (about 40% of the original data set). An inversion of the data set with the modified electrode positions was carried out using the normal approach with a single finite-element mesh. Figure 11c shows the inverse model which is fairly similar to that obtained using the electrodes in their true positions (Figure 11a) with a slightly higher data misfit of 10.9%. The average relative difference in the model values was slightly higher at 1.1% compared to the segmentation method. The largest differences were found in the top layer. A relatively high maximum difference of 46.6% was obtained for a cell in the top layer. This was probably caused by arrays where the electrodes are not equally spaced due to bending of the cable during the survey. Consequently, the electrodes in some configurations were shifted by different amounts with the binning procedure. This resulted in significant changes in the characteristics of the electrode array compared to the true configuration. The binning procedure reduced the calculation time by about 51% which is less than that obtained with the segmentation method (Table 2).

Table 2. Comparison of different methods for the inversion of the Lambayanna field data set.

Inverse method	Number of electrodes	Inversion Time (s)	% model difference Average (Max)	Data misfit (%)
Single mesh	215,873	327,777		10.8
Segments with 8 m buffer zone	215,873	52,731	0.7 (3.9)	10.8
Binning method	87,245	160,611	1.1 (46.6)	10.9

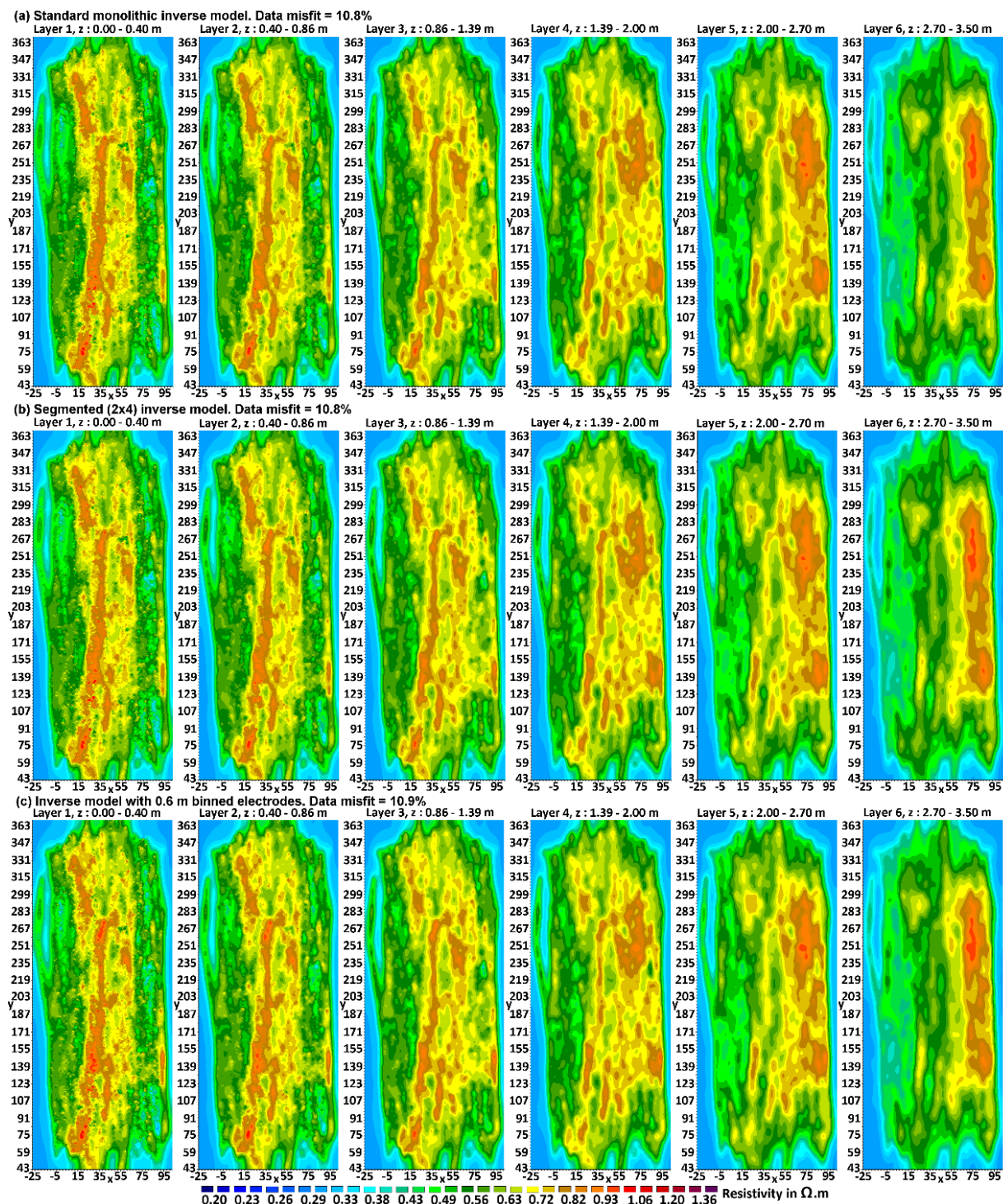


Figure 11. Lambayanna survey inverse models using (a) standard monolithic inversion with a single mesh, (b) 2 by 4 segmented mesh and (c) electrodes binned to every 0.5 m.

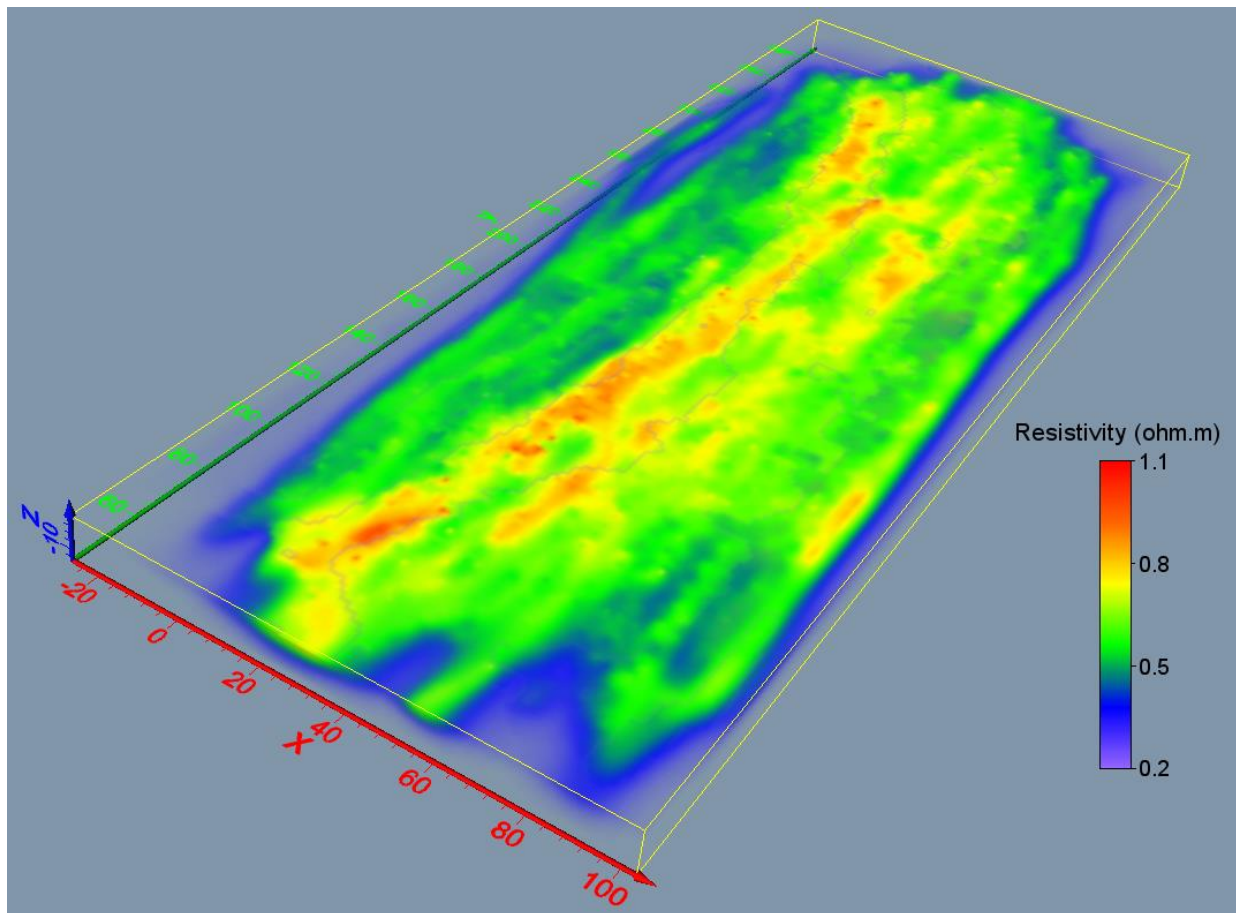


Figure 12. 3-D plot of Lambayanna survey inverse model below the water layer.

DISCUSSION

The use of segments to reduce the calculation time is designed for the inversion of very large data sets with limited computational resources. This situation is frequently encountered by small geophysical companies using personal computers or workstations. In general, a conservative approach is followed that uses the minimum number of segments so that the inversion can be carried out with the available computer resources. It is recommended that the length of a segment should not be less than 5 times the length of the streamer for arrays aligned along the same direction as the side of the segment. As an example, in Figure 11 most of the measurements are in the y-direction using a streamer of 12 metres. Thus, the length of the segments in the y-direction should be at least 60 metres. It is also recommended that the length of a segment in one direction should be not be more than twice the length in the other direction. However, the size and number of segments that provides an optimum balance between reducing the calculation time and accuracy of the results is an area that requires further research.

CONCLUSIONS

Surveys using mobile systems can produce very large data sets with hundreds of thousands of electrode positions and data points. The model used can have hundreds of thousands of cells with a finite-element mesh of more than one million nodes. The segmentation method has proved to be an effective method that reduces the calculation time by more than 80% for very large data sets while producing models with an average difference of

less than 1% from that produced by the standard monolithic approach. An alternative method, binning the electrodes to discrete positions, has the advantage that it is relatively easy to implement. However, in field data sets from mobile surveys where bending of the cable is common, this can cause larger errors in parts of the inverse model (particularly near the surface) compared to the segmentation method. The segmentation method is faster but more difficult to implement. It has been used successfully for surveys with more than half a million electrode positions (Unrau 2019). This makes it practical to carry out the inversion of very large data sets on common and inexpensive microcomputers used by small companies and institutions.

We are currently investigating other techniques to further reduce the calculation time such as directly calculating the Jacobian values at selected cells within a segment that are likely to have significant amplitudes (Papadopoulos *et al.* 2011) and using a homogeneous model approximation for the rest. We are also examining ways to adapt the techniques described in Yang *et al.* (2014), such as the use of local meshes and data subsets, to further reduce the computer time and memory required to process very large resistivity data sets.

ACKNOWLEDGEMENTS

The authors from GeoSat ReSeArch lab express their acknowledgements to Dr. Julien Beck for the fruitful and constructive collaboration in the 2016-2019 during the archaeological project in the Bay of Kiladha which a collaboration between the University of Geneva, under the aegis of the Swiss School of Archaeology in Greece, and the Greek Ephorate of Underwater Antiquities. Wilkinson publishes with the permission of the Executive Director, British Geological Survey (UKRI-NERC). We would like to thank two anonymous reviewers and the Associate Editor for their constructive comments that have helped to improve the paper.

References

- Blome, M., Maurer, H. & Greenhalgh, S., 2011. Geoelectric experimental design -Efficient acquisition and exploitation of complete pole-bipole data sets. *Geophysics*, **76**, F15–F26.
- Christiansen A.V., and Auken E., 2004. Optimizing a layered and laterally constrained 2D inversion of resistivity data using Broyden's update and 1D derivatives. *Journal of Applied Geophysics*, **56**, 247-262.
- Dahlin, T. and Loke, M.H., 2018. Underwater ERT surveying in water with resistivity layering with example of application to site investigation for a rock tunnel in central Stockholm. *Near Surface Geophysics*, **16**, 230-237.
- Daubechies I., 1988. Orthonormal bases of compactly supported wavelets. *Commun. Pure Appl. Math.*, **41(7)**, 909–996.
- Davis K. and Li K., 2013. Efficient 3D inversion of magnetic data via octree-mesh discretization, space-filling curves, and wavelets. *Geophysics*, **78**, 1942-2156.
- deGroot-Hedlin C. and Constable S., 1990. Occam's inversion to generate smooth, two-dimensional models from magnetotelluric data. *Geophysics*, **55**, 1613-1624.
- Dey, A. & Morrison, H.F., 1979. Resistivity modeling for arbitrarily shaped three-dimensional structures. *Geophysics*, **44**, 615–632.

- Edwards L.S., 1977. A modified pseudosection for resistivity and induced-polarization. *Geophysics*, **42**, 1020-1036.
- Farquharson C.G. and Oldenburg D.W., 1998. Nonlinear inversion using general measures of data misfit and model structure. *Geophysical Journal International*, **134**, 213-227.
- Farquharson C.G. and Oldenburg D.W., 2004. A comparison of automatic techniques for estimating the regularization parameter in non-linear inverse problems. *Geophysical Journal International*, **156**, 411-425.
- Hildes D., Dziuba F. and Power M., 2005. Kimberlite Exploration Using a Capacitive-Coupled Resistivity System. *Proceedings of 2005 CSEG National Convention*, May 16-19 2005, Calgary, Canada, 393-395.
- Kuras O., Beamish D., Meldrum P.I., and Ogilvy R.D., 2006. Fundamentals of the capacitive resistivity technique. *Geophysics*, **71**, G135–G152.
- Li, Y. and Oldenburg, D.W., 2000. 3-D inversion of induced polarization data. *Geophysics*, **65**, 1931-1945.
- Li Y. and Oldenburg D.W., 2003. Fast Inversion of large-scale magnetic data using wavelet transforms and logarithmic barrier method. *Geophysical Journal International*, **152**, 251 - 265.
- Loke M.H. and Barker R.D., 1996. Practical techniques for 3D resistivity surveys and data inversion. *Geophysical Prospecting*, **44**, 499-523.
- Loke M.H., 2000. Topographic modelling in resistivity imaging inversion. 62nd EAGE Conference & Technical Exhibition Extended Abstracts, D-2.
- Loke M.H., Acworth I. and Dahlin T., 2003. A comparison of smooth and blocky inversion methods in 2D electrical imaging surveys. *Exploration Geophysics*, **34**, 182-187.
- Loke M.H. and Lane J.W., 2004. Inversion of data from electrical resistivity imaging surveys in water-covered areas. *Exploration Geophysics*, **35**, 266-271.
- Loke M.H., Chambers J.E., Rucker D. F., Kuras O. and Wilkinson P. B., 2013a. Recent developments in the direct-current geoelectrical imaging method. *Journal of Applied Geophysics*, **95**, 135-156.
- Loke, M.H., Frankcombe, K. and Rucker, D.F., 2013b. The inversion of data from complex 3-D resistivity and I.P. surveys. 23rd International Geophysical Conference and Exhibition, 11-14 August 2013 - Melbourne, Australia.
- Loke M.H., Dahlin T. and Rucker D.F., 2014a. Smoothness-constrained time-lapse inversion of data from 3-D resistivity surveys. *Near Surface Geophysics*, **12**, 5-24.
- Loke, M.H., P. B. Wilkinson, P.B., Uhlemann, S.S., Chambers, J.E. and Oxby, L. S., 2014b. Computation of optimized arrays for 3-D electrical imaging surveys. *Geophysical Journal International*, **199**, 1751-1764.
- Loke M.H., Wilkinson P.B., Chambers J.E., Uhlemann S.S. and Sorensen J.P.R., 2015. Optimized arrays for 2-D resistivity survey lines with a large number of electrodes. *Journal of Applied Geophysics*, **112**, 136-146.
- Loke M.H., Wilkinson P.B., Chambers J. E. and Meldrum P.I., 2018. Rapid inversion of data from 2-D resistivity surveys with electrodes displacements. *Geophysical Prospecting*, **66**, 579-594.
- McGillivray P.R. and Oldenburg D.W. 1990. Methods for calculating fréchet derivatives and sensitivities for the non-linear inverse problem : a comparative study. *Geophysical*

Prospecting, **38**, 499-524.

- Oikonomou D., Papadopoulos N., Simyrdanis K., Cantoro G., Beck J. and Loke M.H., 2019. Processing strategies for 3-D marine dynamic electrical resistivity tomography data. 13th International Conference on Archaeological Prospection, 28 August to 1 September 2019, Sligo, Ireland.
- Papadopoulos, N.G., Tsourlos P., Papazachos C., Tsokas G.N., Sarris A. and Kim J.H., 2011. An algorithm for fast 3D inversion of surface electrical resistivity tomography data: application on imaging buried antiquities. *Geophysical Prospecting*, **59**, 557-575.
- Press, W.H, Teukolsky, S.A., Vetterling, W.T. and Flannery, B.P., 2007. Numerical Recipes: The Art of Scientific Computing (3rd Edition). Cambridge University Press.
- Rucker, D.F., Levitt, M.T. and Greenwood, W.J., 2009. Three-dimensional electrical resistivity model of a nuclear waste disposal site. *Journal of Applied Geophysics*, **69**, 150-164.
- Rucker D.F. and Noonan G.E., 2013. Using marine resistivity to map geotechnical properties: a case study in support of dredging the Panama Canal. *Near Surface Geophysics*, **11**, 625-637.
- Sasaki Y., 1989, Two-dimensional joint inversion of magnetotelluric and dipole-dipole resistivity data. *Geophysics*, **54**, 254-262.
- Silvester P.P. and Ferrari R.L., 1990. Finite elements for electrical engineers (2nd. ed.). Cambridge University Press.
- Simyrdanis K., Papadopoulos N., Kim J.H., Tsourlos P. and Moffat I., 2015. Archaeological Investigations in the Shallow Seawater Environment with Electrical Resistivity Tomography. *Journal of Near Surface Geophysics, Integrated geophysical Investigations for Archaeology*. **13**, 601- 611.
- Spitzer K., Chouteau M. and Boulanger O. 1999, Grid-independent electrode positioning for 3D DC and IP forward modelling. Proc. 2nd. Internat. Sym. 3D Electromagnetics, 189–192.
- Tsourlos P., Papadopoulos N., Papazachos C., Yi M.Y. and Kim J.H., 2014. Efficient 2D inversion of long ERT sections. *Journal of Applied Geophysics*, **105**, 213-224.
- Unrau T., 2019. Towed Capacitively Coupled Resistivity Systems in Arctic Exploration - Advances in Equipment Design and Handling of Very Large Resistivity Surveys. AGU 100 Fall Meeting, San Francisco, 9-13 Dec. 2019, NS22A-07.
- Xu, T. and Dunbar, J.A., 2015. Binning method for mapping irregularly distributed continuous resistivity profiling data onto a regular grid for 3-D inversion. *Journal of Environmental and Engineering Geophysics*, **20**, 1-17.
- Yang, D., Oldenburg, D.W. and Haber, E., 2014. 3-D inversion of airborne electromagnetic data parallelized and accelerated by local mesh and adaptive soundings. *Geophysical Journal International*, **196**, 1492–1507.
- Zhou B. and Dahlin, T., 2003. Properties and effects of measurement errors on 2D resistivity imaging surveying. *Near Surface Geophysics*, **1**, 105-117.

Appendix : Using the Discrete Wavelet Transform

This section describes the practical use of the Discrete Wavelet Transform (DWT). While the Fast Fourier Transform (FFT) is based on the sine and cosine functions, the DWT is based on the ‘mother wavelet’ function (Daubechies 1992). The sine and cosine functions are localised in frequency (but not in space or time). In comparison, the wavelet functions are localised both in frequency and space. This makes them useful for functions such as the Jacobian data series (Figure 7a) that exhibit a quasi-periodic structure over a limited interval near the electrodes. Press *et al.* (2007) gives a description of the wavelet functions, together with wavelet filter coefficients and computer code to carry out the wavelet transform. Like the FFT, the computer implementation of the DWT is optimized for a data vector where the number of points is an integer power of 2. The number of model cells for the example in Figure 7a is 1575. In calculating the DWT, the data series is extended to 2048 by padding the end with zeros. The time taken by the DWT is proportional to $m \cdot \log(m)$ where m is the length of the data vector. The time taken by the DWT to calculate the transform for the Jacobian matrix is only a few percent of the overall time taken to invert the data set. It is in fact less than time taken to read the Jacobian values from (and write the transformed values to) the computer hard-disk.